Numerical Investigations of Model Support Interference in Subsonic and Transonic Wind Tunnels

Sylvain Mouton

NUMERICAL INVESTIGATIONS OF MODEL SUPPORT INTERFERENCE IN SUBSONIC AND TRANSONIC WIND TUNNELS

S. Mouton[*]

[*] Office National d'Etudes et de Recherches Aérospatiales (ONERA), Applied Aerodynamics Department
BP72 - 29 Avenue de la Division Leclerc, 92322 Châtillon Cedex, France

Key words: Aerodynamic, wind tunnel, sting, strut, support interference

Abstract: *The aerodynamic interference effects of usual devices supporting aircraft models during wind tunnel tests have been studied by means of steady RANS simulations of the flow. The flow field and force disturbance caused by the supports were deduced by comparing simulations with and without support. Two configurations were addressed. The first one deals with low speed test of a large transport aircraft mounted on a circular strut. Only longitudinal forces on a clean configuration are studied. The second one deals with transonic test of a business jet model mounted on a Z-sting. The support effect is analysed for several Mach numbers and angles of attack. Special attention was paid to the proper derivation of corrections of the incoming flow conditions in terms of Mach number and angle of attack. Comparison against experimental data is provided to validate the results.*

NOMENCLATURE

α	Angle of attack
CA	Axial force coefficient
CD	Drag force coefficient
CL	Lift force coefficient
CN	Normal force coefficient
Cm	Pitching moment coefficient
Cp	Pressure coefficient $Cp = \frac{p - p_{ref}}{q_{ref}}$
M	Mach number
p	Static pressure
q	Dynamic pressure
S_{CS}	Area of model cross-section
S_F	Area of fuselage cross-section
X	Distance to the PMR along wind tunnel axis
x	Distance to the PMR along model axis

$\delta\xi$	Difference of field quantity ξ due to the support $\delta\xi = (\xi)_{support\ on} - (\xi)_{support\ off}$
$\Delta\xi$	Difference of integral quantity ξ due to the support $\Delta\xi = (\xi)_{support\ on} - (\xi)_{support\ off}$
Subscripts	
∞	Flow state at entry of the computational domain
f	Friction
ff	Far-field
nf	Near-field
p	Pressure
ref	Flow state near model position, reference quantity
Abbreviations	
AoA	Angle of Attack
CFD	Computational Fluid Dynamics
HTP	Horizontal Tail Plane
PMR	Point of Model Rotation
SCAB	Sting Calibration Body

1. INTRODUCTION

During wind tunnel tests the aircraft model is maintained in the test section thanks to a support system. This support is shaped to be as small and as discreet as possible, under the constraint that it should sustain forces generated by usual types of models over a wide range of flow conditions and enclose all cables and tubes necessary to supply energy and collect measurements from the embarked sensors. These constraints may in fact lead to large size supports compared to the model dimensions, especially in pressurized wind tunnels where the forces on the model can reach several tons. Therefore, it is generally recognized that aerodynamic interference caused by the model support may have a significant effect on the measured data [2][8] and several studies were undertaken in the past decades [12][13][16] to determine this effect for numerous configurations and flow velocity.

In most wind tunnel procedures, the support effect is now accounted for thanks to various corrections methods [7][14][17][21]. Unfortunately, the presently existing methods exhibit several drawbacks [3]:

- they differ from one wind tunnel to another, making it difficult to compare final results;
- they rely on simplifying hypotheses and/or empirical assumptions, which validity is doubtful for example at high Mach numbers or for unconventional models;
- they call upon dedicated experiments which are touchy, expensive and requires the introduction of another support, i.e. additional distortions of the flow.

In an attempt to alleviate these drawbacks, several recent [6][10][15] or older [4] initiatives aimed at determining whether advanced numerical simulations could help in understanding and predicting the support interference effect. In this paper, two examples of such investigations carried out at ONERA are presented. The first one deals with low-speed single-strut interference on longitudinal forces on an Airbus configuration tested in the F1 wind tunnel. The second application presents results obtained on a Dassault Aviation Falcon mounted on a Z-sting at ETW at cruise conditions.

Note that the support is generally called a 'sting' when nearly lined up with the oncoming flow or a 'strut' when more or less vertical, and this nomenclature will be used throughout this paper. A sting is very often attached to a

'sector' that enables AoA variations.

2. SINGLE STRUT EFFECT AT LOW-SPEED

A test campaign dedicated to the assessment of interference effects of the usual systems supporting the model was carried out in the ONERA F1 wind tunnel at Le Fauga-Mauzac using an Airbus model. It confirmed the existence of significant effects on the measurement of model forces, as was previously studied by means of experiments and computations on aircraft [11][20] or helicopter [9][19] models. The results gained served as a basis for correction laws that are believed to be satisfactory. However, testing other models would require performing new tests to derive accurate support effects. To avoid such expensive tests, CFD is foreseen as an appropriate way to predict support effects. The work then undertaken and reported in this section aimed at validating the ability of RANS CFD tools to predict the effect of the single strut on pressure distribution and on model forces.

2.1. Test case, experiments and flow modelling

The Airbus model was tested in the F1 wind tunnel [7] to investigate the interference effect of a single circular strut of diameter 80 mm at the model entry and increasing to 120 mm closer to the bottom wall. The size of the test section was 3.5×4.5 m, the frontal area of the strut was 0.180 m^2 and the span of the model was 2.869 m. The hydraulic diameter of the fuselage ($2\sqrt{S_F/\pi}$) was 300 mm, i.e the ratio of the strut diameter to the fuselage diameter was 0.27, which should yield moderate disturbance according to [11]. As shown in Figure 1, this model was tested mounted on a fin sting. Measurements were first carried out without any strut to acquire reference data. A dummy strut was then mounted in the test section and measurements were performed at 10 fixed angles of attack, the strut position being each time adjusted to keep in same relative position the model and its dummy support. The whole campaign was realised with a Mach number of 0.20 and a Reynolds number of 7.7 millions based on mean aerodynamic chord.

The modelling of this test campaign for CFD was realised only for the clean configuration (slats and flaps retracted). The body, the wing, the horizontal tail plane (HTP) and the strut were included in the model. The main remaining differences with the real model tested were:

- the through flow nacelles, their pylon and the flap track fairings were not modelled;
- the fin sting support was replaced by the real vertical tail plane;
- the unsealed gap between the strut and the edge of the fuselage hole was not modelled because of the lack of proper geometrical data. Note however that this gap was reported to have an effect on pressure distribution because of flow leakage [19].

The turbulent boundary layer is modelled on the aircraft skin and on the strut surface thanks to boundary conditions and proper refinement of the mesh. On the contrary, no viscous effect is modelled on the wind tunnel walls, which allowed us to keep them parallel and to extend the test section up and downstream by about 5 times the length of the model.

A structured mesh comprising around 8 millions nodes was build around the model and strut and is shown in Figure 2. For computations without strut, new blocks of mesh are added to fill in the volume of the strut, so that no alteration is made to the rest of the mesh. It ensures that spurious differences resulting from a mesh effect are kept as low as possible, and it allows accurate comparison of the flow fields on the model skin and in the surrounding volume.

The physical model implied compressible RANS equations and the two-equation k-ω turbulence closure of Menter, with Zheng limiter. This turbulence model has been selected thanks to preliminary computations on a 2D cylinder, compared to experiments reported in [1]. The main numerical parameters are summarized below:

- Mean flow equations were solved thanks to a Jameson second order spatial scheme. Coefficients of artificial dissipation for second and fourth order are respectively $\xi_2 = 0$ and $\xi_4 = 0.008$. Martinelli correction was used with an exponent of 0.3;
- Equations for turbulence field were solved thanks to a first order Roe scheme, with Harten correction using a factor of 0.01;
- Low speed preconditioning of Chow & Merkle, with parameter $\beta = 5$ for the preconditioning of convective fluxes and $\beta = 1$ for the preconditioning of artificial dissipation was used;
- Iterative method for time marching was a first order backward Euler scheme, associated with implicit scalar LU-SSOR solving with 4 relaxation cycles;
- To improve convergence, local timestep and a 2-level multigrid cycle were used.

2.2. General results

Computations were realised with *elsA* software [5], on two processors of ONERA vector computer NEC SX-8. 2,000 iterations representing about 14 hours CPU time were necessary to reach convergence on configuration without strut, with the L_2-averaged mean flow residuals loosing 4 orders of magnitude and efforts well stabilised. Concerning the configuration with strut, natural unsteadiness of the flow prevented the computation to reach such a fully converged state. Residuals were brought down by only 2.5 orders of magnitude, and forces kept oscillating around a stabilized mean value, with $\pm 2\ 10^{-4}$ *CD*, $\pm 3\ 10^{-3}$ *CL* and $\pm 3\ 10^{-3}$ *Cm* amplitude. An attempt to damp these oscillations thanks to higher artificial dissipation ($\xi_4 = 0.032$) was successful, resulting in an identical increase of drag and lift for the configuration with strut and without strut, predicting therefore identical strut effect. Consequently, because these

oscillations are representative of the flow physics, it was preferred to work with lower artificial dissipation and to rely on the force coefficients averaged over the last 500 iterations.

Corrections were applied to the force coefficients and to the upstream Mach number and AoA to account for wall interference effect. The set of correction used was the same for experimental and for CFD data, and was computed according to usual wind tunnel procedure [7][21]. Blockage correction due to the support was applied neither on experimental data nor on simulation data. The figures presented in this paper do not include the force on the vertical tail plane that was not present during wind tunnel test.

The Figure 3 shows a comparison between computed and measured force coefficients. This comparison is not fully rigorous since the nacelles and flap track fairings were not present in the computation. Consequently, the computed drag coefficient is lower by about 50 10^{-4}. The lift gradient is slightly underestimated. The aerodynamic centre is predicted 4% of mean chord away from its measured position. Apart from the above discrepancies, general agreement is good.

2.3. Strut effect on the flow and on model forces at iso-AoA

In this section, the strut effect is regarded as the difference between configuration with strut and configuration without strut, the geometrical AoA of the model being kept constant between the two configurations, which can be summarized as:

$$\left.\begin{array}{l}\Delta\alpha = 0\\ \Delta CN\\ \Delta CA\\ \Delta Cm\end{array}\right\} \text{computed}$$

The effect on the flow is first examined on the skin of the model by observing in Figure 4 the difference in pressure distribution δC_p. This quantity is compared to the experimental data collected thanks to the pressure taps indicated by the dots on the lower part of the figure. The interpolation of the experimental data on the skin was realised thanks to a Kriging method. The interpolation is accurate on most parts of the fuselage where the pressure gradient is small with regard to the spacing of the sensors. This is not the case close to the strut-fuselage junction, where interpolated contour lines should be disregarded.

The distribution of pressure disturbance created by the strut is similar to the pressure distribution around an isolated cylinder, with a stagnation point on the fore part and a separated region of low pressure on the aft part. It weakly depends on the AoA. Alteration of the wing flow is related to an increase of local AoA over the whole wing span. Compared to the available experimental data, the pressure disturbance is well predicted upstream of the strut. On the opposite, disturbance related to the strut wake is not accurately predicted. The suction on the aft part of the strut is underestimated like in the 2D cylinder computations that were performed to select the turbulence model. More downstream, the computation predicts an area of positive δC_p corresponding to the end of the recirculation area that is observed in experiment roughly at the same position. The rest of the wake exhibits slightly negative δC_p (around -0.03) that are underestimated by the computation (around -0.01).

The strut effect on forces can be observed in Figure 5. Computations predict that the strut increases the lift coefficient of the model by about 0.01 whatever the angle of attack, whereas experiments show a dependency with the angle of attack, however with widely scattered measurements. This effect is also lower than the one reported in [11], with the same support but on a different model. The effect of the strut on axial force is very well predicted, and remains within experimental uncertainties at all computed angles of attack. Finally, the effect on pitching moment coefficient is underestimated by around 0.005. Its order of magnitude is the same as in [11]. In general, regarding the available experimental dataset, the strut effect is accurately predicted all over the range of angle of attack studied.

The strut effect was examined on each part of the model and the result is shown in Figure 6. The upwash on the wing is the main responsible for the lift increase. It has also a direct effect on the axial force, but only a minor contribution to pitching moment due to the fact that the reference point is located close to the wing aerodynamic centre. According to the observed wing lift increment, and considering the slope of the wing lift curve, the mean upwash on wing is 0.15º, in line with the value derived in [20]. Similarly, the downwash on the HTP plays a role on lift and axial forces, but with smaller amplitude because of the smaller size of the lifting surface and because of the smaller $\delta\alpha$ at the HTP location. On the opposite, due to the lever arm, the HTP is a major contributor to pitching moment. The magnitude of +0.005 for ΔCm_{HTP} is in agreement with value obtained by comparing tests results with and without HTP. The impact of the large flow disturbance at the strut-fuselage junction is responsible for fuselage contribution to drag and pitching moment. Finally, the variation of friction drag is negligible on every part of the aircraft.

2.4. Strut effect on the flow and on model forces at iso-Lift

Since the wing obviously suffers from the upwash created by the support and since it contributes to the lift and drag deviations, the idea of correcting the AoA to account for support interference was put forward. Computations were then undertaken to compare ΔCD and ΔCm at iso-lift instead of iso-AoA. Contrary to the previous sub-section, $\Delta\alpha$ is now computed to ensure $\Delta CN = 0$ (lift is here approximated by normal force) and according to the slope of the lift curve, the geometrical AoA of the model in the tunnel is then decreased by $\Delta\alpha = 0.115$º. This can be summarised as:

$$\left.\begin{array}{l}\Delta CN = 0\\ \Delta\alpha\\ \Delta CA\\ \Delta Cm\end{array}\right\} \text{computed}$$

The effect on the flow close to the fuselage is very similar to the case at iso-AoA visible in Figure 4. The wing is still subjected to upwash on its inboard part, but this is partly compensated by the outboard part lying in a region of negative $\delta\alpha$.

The force breakdown is displayed in Figure 7 for the three studied lift conditions. The effect of the strut on fuselage forces is nearly unchanged compared to the iso-AoA computation. Because of the more negative angle of attack, the down force generated by the HTP is slightly larger, with coherent effect on axial force and pitching moment. In spite of the AoA reduction, the lift of the wing with strut remains higher than without strut, so as to compensate for the down force on HTP. The ΔCN on wing was however significantly reduced, with associated reduction of ΔCA by 30% to 60%. Note that if the iso-lift definition of the strut effect is selected, forces have to be projected in wind axes using the corrected AoA $\alpha_{ref} = \alpha_\infty - \Delta\alpha$ to be consistent.

2.5. Conclusion

Steady RANS computations were performed on the model shape tested at F1, and compared to the available exhaustive experimental database. In spite of inaccuracies in the prediction of the strut wake, the ability of this modelling to predict the strut effect on pressure distribution and on model forces was demonstrated. A breakdown of the force acting on the different parts of the model was realised and showed the contribution of each element to the total interference effect. The flow on wing and HTP is altered by up- and down-wash. Consequently, the wing is a major contributor to the strut effect. This can be partly compensated by altering the angle of attack of the model with strut. The fuselage has a significant contribution only to drag and pitching moment. HTP has mostly an effect on pitching moment.

3. Z-STING SUPPORT EFFECT UNDER TRANSONIC CONDITIONS

This second application deals with high Reynolds transonic test of a Falcon model in the cryogenic wind tunnel ETW near Cologne [23]. Contrary to the previous case, no twin sting test were available to asses the effect of the support. Therefore, no validation of the predicted sting effect could be realised. Additionally, ETW has a test section of 2.0×2.4 m, with solid lateral walls and slotted top and bottom walls. Since no satisfying solution was found to model the slotted wind tunnel walls, all computations presented below were realised in free flow, i.e. without any modelling of the tunnel walls.

3.1. Mach number and AoA corrections

The transonic flow over supercritical airfoils is well known to be very sensitive to the Mach number and AoA, which drives the position of the shock wave on the upper side. This is the reason why accurate Mach number and AoA corrections should be used to compensate for support disturbance, not only in the wind tunnel but also in the computation. This section presents the procedure that was used to determine these corrections.

For each Mach number and AoA, a preliminary computation was realised, consisting in an Euler computation of the flow on the isolated Z-sting (without the blade). Mach number and AoA deviations are then probed at the point of model rotation (PMR), which in most test cases corresponds to the longitudinal position of the 25% of mean aerodynamic chord. Figure 8 shows the results obtained for Mach 0.80 to 0.90.

One can observe that the support slows the Mach number down by a few 10^{-3} at the PMR. This velocity disturbance increases with Mach number in agreement with Prandtl-Glauert compressibility rule. It is independent of the AoA in the small range we were interested in. Concerning flow angle, because the support mainly lies below the model centreline, it deviates the oncoming flow upwards. The order of magnitude of resulting upwash at the PMR is of some hundredth of a degree and it decreases with Mach number. The order of magnitude of these values is in agreement with previous findings on similar supports [8][21][22].

The values of ΔM and $\Delta\alpha$ of Figure 8 were used to correct upstream flow conditions in the computation of the model with support as indicated in Figure 9. One should note that in all cases, p_{ref} and q_{ref} are used to compute the pressure and force coefficients, whereas some authors [8] compute coefficients with upstream conditions p_∞ and q_∞ and apply afterward a dynamic pressure correction factor. Similarly, and contrary to section 2 where several definitions of sting effect were investigated, the angle used to project the force vector onto wind axes is always α_{ref} and not α_∞.

3.2. Validation against sting calibration data

To assess the accuracy of the isolated sting computation and to gain insight into the validity of the derived ΔM and $\Delta\alpha$, a comparison with experimental data gathered during tests with the sting calibration body (SCAB) was performed.

The SCAB is an axisymmetrical body of diameter 160 mm, with a sharp nose and a base. It was mounted on the Z-sting support used for the Falcon model resulting in the configuration shown in Figure 10. Results are also available from previous tests with the SCAB mounted on straight sting. From ETW experience, such configurations are insensitive to Reynolds effect [18]. Euler Chimera computations were then performed with *elsA* software to simulate the

SCAB in the following configurations: isolated, mounted on straight sting, in the presence on Z-sting without blade and mounted on Z-sting with blade. Flow separation on the base of the SCAB is not accurately predicted with such inviscid modelling, but is not of interest here.

Results on this configuration are presented in Figure 11 at Mach 0.85, showing distribution of pressure on the top, side and bottom of the SCAB. First of all, one can notice that although the tunnel walls and sector were not modelled, no systematic deviation between experiments and computation is observed. This indicates that the wind tunnel walls do not generate significant pressure gradient, i.e. their divergence is properly set to compensate for boundary layer growth and also probably for the gradient generated by the sector [10]. It also shows the efficiency of the slots in preventing blockage effects for this non-lifting case. Secondly, the Figure 11 shows that the slowdown effect of stings on the oncoming flow extends far away from the support, and covers the entire model. Finally, by comparing pressure distribution for straight sting and Z-sting to reference distribution on the isolated SCAB, it appears that the Z-sting support generates larger velocity slowdown than the straight sting, yielding for example $\Delta M = -4.9\ 10^{-3}$ at the PMR instead of $-2.6\ 10^{-3}$. This disturbance becomes locally even larger ($-7.9\ 10^{-3}$) when considering the blade.

The computation procedure described in Figure 9 relies on the pressure distribution created by the Z-sting without blade. It was checked that the computation on isolated support yields the same pressure distribution than the difference between SCAB on support and SCAB alone (apart from stagnation regions), which proves that we are in the scope of linearised potential theory. This justifies the use of isolated sting computation in the procedure. From Figure 11, it can be seen that the Mach number correction deduced from this procedure is underestimated by about $3\ 10^{-3}$ at the PMR because it does not account for the blade.

3.3. Breakdown of sting effect

Comparing the force on the model without sting and the force on the model with sting and with properly corrected upstream conditions yields the total sting effect, as sketched in Figure 9. A breakdown of this effect on drag is then proposed, after [8] and [17], between far-field and near-field effect. The far-field effect is defined as a force due to a pressure disturbance $\delta\hat{C}\mathrm{p}$ which gradient is assumed to be directed along the model centreline. If this gradient linearly adds to the field generated by the model, it creates a force in the axial direction known as buoyancy force and which coefficient is expressed as:

$$\Delta CD_{\mathrm{ff}} = -\int_{\substack{\text{Model}\\ \text{centreline}}} \frac{d\delta\hat{C}\mathrm{p}}{dx}\frac{S}{S_{\mathrm{ref}}}dx.\cos\alpha_{\mathrm{ref}}$$

At small AoA, $\cos\alpha_{\mathrm{ref}} \approx 1$ and in practice the axial force is confused with drag force. To compute this buoyancy force, the pressure distribution $\delta\hat{C}\mathrm{p}(x)$ is the one probed along the model centreline in the isolated sting computation. The resulting force ΔCD_{ff} is presented in Figure 15 and ranges between -5 and $-8\ 10^{-4}$. This force is subtracted from the total sting effect to give the near-field effect.

The use of far-field correction has to be defined in accordance with the wind tunnel procedure. A buoyancy correction is already part of the usual data reduction performed in most wind tunnels. Therefore, care has to be taken not to account for it twice, by applying first usual wind tunnel corrections, and then support corrections deduced by CFD. In the present case, buoyancy was corrected by ETW based on experimental data, and only the near-field effect was used as a CFD support correction.

3.4. Flow computations and sting effect

Flow on the Falcon model, with and without support, was computed including the modelling of the following features (see Figure 12):

- Full aircraft model, including body, wing (shape under cruise lift coefficient), lateral and central nacelles, vertical and horizontal tail planes.
- Connecting elements (blade, sting, sting boss) down to the sector attachment. The sting is prolonged down to the infinite downstream by a cylinder of diameter 445 mm. The clearance between the blade and the model is considered as perfectly sealed and is consequently not modelled.

The Reynolds number based on mean aerodynamic chord was $16\ 10^{6}$ for all computations, identical to the test. The boundary layer was regarded as fully turbulent. Computed Mach numbers were 0.80, 0.85 and 0.90.

A structured grid was built around this geometry. Taking advantage of *elsA* capabilities to deal with partially and totally non-matching joins between blocks, the mesh size could be limited to about 7 millions cells while maintaining good refinement in places of interest. It is estimated that a gain of about 35% compared to fully coincident grid was realised on this case. Like in previous section, the volume of sting and blade was filled with new blocks of mesh for computations without support so as to minimize spurious effect. Compressible RANS equations were solved using *elsA* software [5]. The two-equation k-ω turbulence closure of Wilcox, with Kok correction, Zheng limiter and production of k based on vorticity was used. The main numerical parameters were the same as in 2.1, except for the low-speed preconditioning that was not used at the studied transonic conditions. 1,500 iterations realised on a NEC SX-6 representing 21 hours CPU were necessary to reach convergence. L_2-averaged mean flow residuals lost 4 orders of magnitude and efforts were stable within $\pm 0.2\ 10^{-4}$ *CD*, $\pm 10^{-3}$ *CL* and $\pm 10^{-3}$ *Cm*.

The Z-sting support effect on the pressure distribution on the model surface may be observed in Figure 13. First, one can note that the Mach number correction applied was rather successful in retrieving correct Mach number near the

wing of the model, at the cost of a slight overspeed on the nose. Plotting the flow angle in the volume surrounding the model shows qualitatively that the AoA corrections also permitted to compensate for support-induced upwash. As a consequence, the wing shock wave is not moved by the support interference, as can clearly be seen in Figure 14. The larger distortions are logically observed close to the blade, but they also extend to the lateral nacelles where the size of the supersonic region is reduced by the shock wave moving upstream. The flow slow-down associated with the stagnation region at the blade leading edge also extends to the wing lower surface. A shielding effect from the lateral nacelles can be observed resulting in the upper side of the lateral nacelles and the central nacelle suffering almost no distortion. The whole horizontal tail plane lies in a region of overspeed as predicted by SCAB computations reported in Figure 11.

Because no twin sting test result was available on this model, it was not possible to validate these observations against experimental data. However, the test at ETW allowed us to compare computed and measured pressure distribution on 7 sections on the wing. The agreement was found very satisfactory, as shown in Figure 14.

The effect of the sting support on model forces is presented in Figure 15. At first, let us analyse results at Mach 0.80 and 0.85 only. The lift is increased by around $1.5\ 10^{-2}$ nearly independently of the AoA and increasing with Mach number. This is related to the pressure increase on the lower side of wing and fuselage. Concerning drag, the far-field effect lowers the drag of the model because of dominating positive pressure gradient. The remaining near-field effect ranges between -5 and $+5\ 10^{-4}$, and like the effect on lift it grows with Mach number. Negative pitching moment deviation of about -5.10^{-3} accounts for the upwash on the horizontal tail plane. It is weakly dependent on AoA and it is again increasing with Mach number. At Mach 0.90 a shock wave appears on the wing lower surface. It is then not possible to keep shock waves at the right position on both side of the wing when introducing the support. This explains the rapid growth of deviations at this high Mach number.

3.5. Conclusion

Sting interference effect has been computed prior to the transonic test of a Falcon model and could be used as corrections during the test campaign. The magnitude of the effect of the Z-sting support was found weak. The wing flow and especially the shock wave position were nearly unaltered by the support. The larger disturbances appear on the lower side of the lateral nacelles. Special interest was paid to the proper determination of Mach number and AoA corrections to perform computations with support that are comparable to wind tunnel data. A breakdown of drag deviations between near-field and far-field effects was proposed to facilitate the integration of CFD results into the usual wind tunnel corrections.

4. CONCLUSION & PERSPECTIVES

The two applications presented in this paper illustrate possible contributions of CFD to improve the understanding of support interference in wind tunnel tests. Both low speed and high speed test configurations, with different models and supports, were successfully addressed by RANS simulations of the flow. The importance of proper Mach number and AoA corrections prior to performing computations with support was highlighted, and a way to determine these corrections was proposed.

Investigations on support interference are still undergoing as a part of the FLIRET project and other research projects. Special interest is paid to the improvement and the generalisation of the determination of Mach number and AoA correction, both for computations and for experiments. From the design point of view, the experience gained throughout these projects could be used to support the design of low disturbance supports. The rising use of Chimera technique will make considerably easier the meshing process in the near future. The use of other CFD codes relying on unstructured meshes might also be a solution to improve response time and to address more complex configurations.

ACKNOWLEDGEMENT

The author would like to thank the European Commission for funding part of this research work within the FLIRET project. The helpful words of advice of J.F. Piat, A. Mignosi (ONERA), J. Quest and M. Wright (ETW) are gratefully acknowledged.

REFERENCES

[1] E. Achenbach, *Distribution of Local Pressure and Skin Friction around a Circular Cylinder in Cross-Flow up to Re=5×10⁶*, Journal of Fluid Mechanics 34, pp. 625-639, 1968.

[2] P.J. Bobbitt, *The Pros and Cons of Code Validation*, NASA TM 100657, July 1988.

[3] C.P. Brichter, C.W. Alcorn, W.A. Kilgore, *Subsonic Sting Interference on the Aerodynamic Characteristics of a Family of Slanted-Base Ogive-Cylinder*, NASA CR4299, 1990.

[4] R.H. Bush, D.W. Jasper, S.L. Parker, W.W. Romer, P.G. Willhite, *Computational and Experimental Investigation of F/A-18E Sting Support and Afterbody Distortion Effects*, Journal of Aircraft, Vol. 33, No. 2, March-April 1996.

[5] L. Cambier, M. Gazaix, *elsA: An Efficient Object-Oriented Solution to CFD Complexity*, AIAA 2002-0108, Reno, January 14-17, 2002.

[6] R. Collercandy, B. Marquez, J. Lory, S. Dbjay, L. Espiau, *Application of CFD for Wall and Sting Effects*, HiReTT Technical Note HIRETT/TN/AF/RCo/WP2.2/31102003, October 2003

[7] P. Desplas, *F1 Pressurized Subsonic Wind Tunnel User's Guide*, ONERA document, 1998.

[8] A. Elsenaar, S.O.T.H. Han, *A Break-Down of Sting Support Interference Effects*, NLR TP 91220 U, May 1991.
[9] H.F. von Geyr, N. Kroll, *Application of 3D-Preconditioning for the Prediction of Helicopter Fuselage Drag*, 20th European Rotorcraft Forum, Rome, 14-16 September 1999.
[10] A. Heidebrecht, *A Numeric Far Field Model for Support Interference Studies in a Slotted Wall Wind Tunnel (ETW)*, 2nd International Symposium on Integrating CFD and Experiments in Aerodynamics, RMCS Cranfield University, 20 September, 2005.
[11] M. van de Kreeke, M. Quémard, M. Verrière, *The Interference of the Model Support Mast with Measurements of the Longitudinal and Lateral Aerodynamic Coefficients*, NASA TT-20079, 1987.
[12] E.S. Love, *A Summary of Information on Support Interference at Transonic and Supersonic Speeds*, NACA RM L53K12, January 1954.
[13] D.L. Loving, A.A. Luoma, *Sting-Support Interference on Longitudinal Aerodynamic Characteristics of Cargo-Type Airplane Model at Mach 0.70 to 0.84*, NASA TN D-4021, July 1967.
[14] M. Lyonnet, J.F. Piat, B. Roux, *Model Support Interference Assessment using a Metric Rear Fuselage and a Twin-Sting at ONERA S2MA Wind Tunnel*, International Conference on Experimental Fluid Mechanics, Turin, July 4-8, 1994.
[15] M. Maina, N. Corby, E.L. Crocker, P.J. Hammond, P.W.C. Wong, *A Feasability Study on Designing Model Support Systems for a Blended Wing Body Configuration in a Transonic Wind Tunnel*, The Aeronautical Journal, January 2006.
[16] M.H. Tuttle, B.B. Gloss, *Support Interference of Wind Tunnel Models. A Selective Bibliography*, supplement to NASA technical memorandum 81909, May 1984.
[17] J. Quest, *Tunnel Corrections in ETW*, ETW Technical Memorandum ETW/TM/99024, March 1999.
[18] J. Quest, M. Wright, S. Rolston, *Investigation of a Modern Transonic Transport Aircraft Configuration over a Large Range of Reynolds Numbers*, AIAA 2002-0422, Reno, January 14-17, 2002.
[19] T. Renaud, D. O'Brien, M. Smith, M. Postdam, *Evaluation of Isolated Fuselage and Rotor-Fuselage Interaction using CFD*, 60th American Helicopter Society Annual Forum, Baltimore, 7-10 June 2004.
[20] M. Saiz, C. Quémard, *Essais dans la soufflerie F1 de l'ONERA, comparaison vol-soufflerie*, paper no. 22 in Wind Tunnels and Testing Techniques, AGARD CP-348, 1984.
[21] X. Vaucheret, *Recent Calculation Progress on wall Interferences in Industrial Wind Tunnels*, La Recherche Aérospatiale, no. 3, pp 45-57, 1988.
[22] X. Vaucheret, *Expected improvements on High Angle of Attack Model Testing*, AGARD/FDP Symposium, Munich, 5-7 May 1980.
[23] U. Walter, *ETW User Guide*, Report number ETW/D/95001/A, February 2005.

FIGURES

Figure 1: Airbus model during test with dummy strut at F1

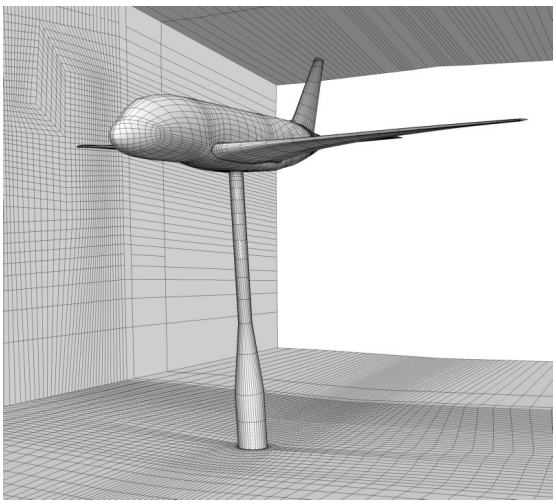

Figure 2: Mesh of the model and its support in the test section (1 mesh point out of 4 is displayed)

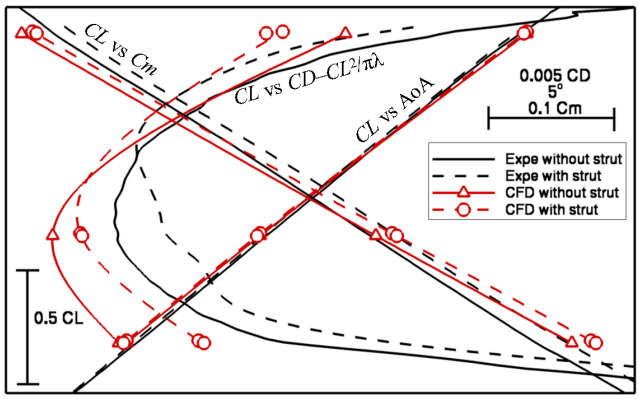

Figure 3: Comparison of lift, drag (wing elliptic induced drag removed) and pitching moment coefficient with and without strut, as measured and computed – forces are projected on AoA not corrected for strut effect

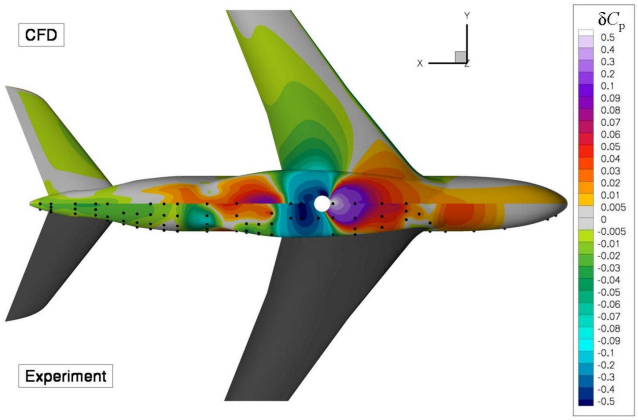

Figure 4: Strut effect on pressure distribution under the Airbus model at AoA 10º as computed (top) and measured (bottom, dots indicate pressure taps)

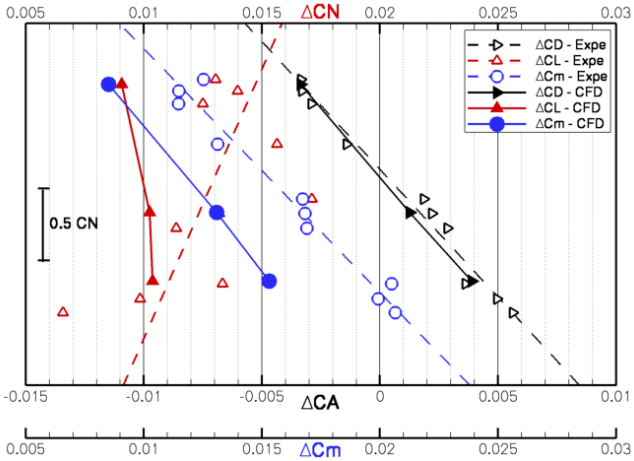

Figure 5: Strut effect on forces

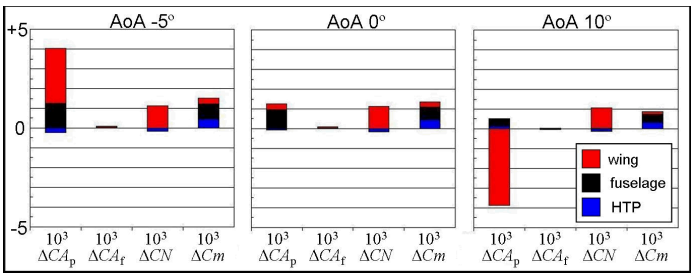

Figure 6: Breakdown of strut effect at iso-AoA

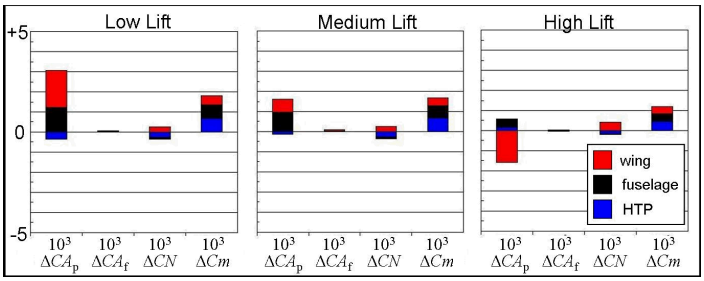

Figure 7: Breakdown of strut effect at iso-Lift

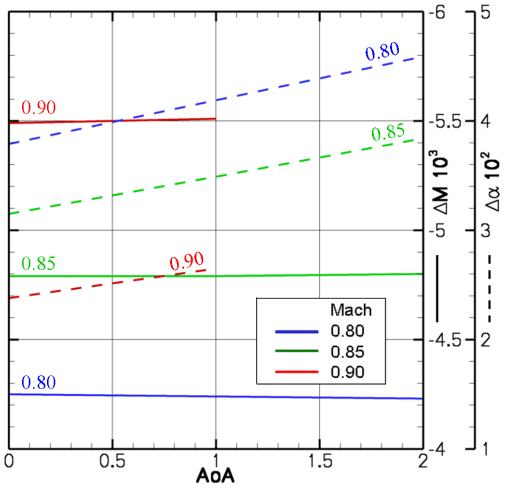

Figure 8: Mach number(continuous lines) and AoA (dashed lines) deviations at PMR deduced from sting alone Euler computations

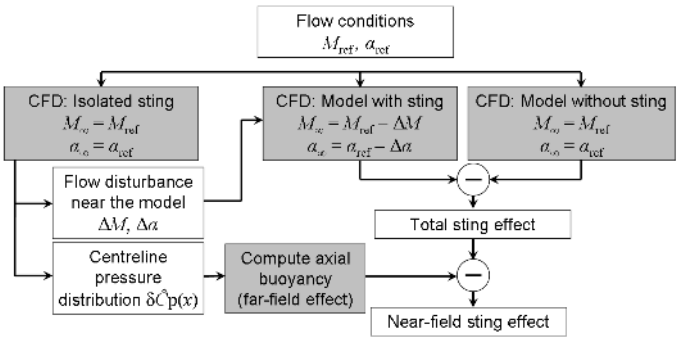

Figure 9: Computation procedure for the prediction of transonic sting effect

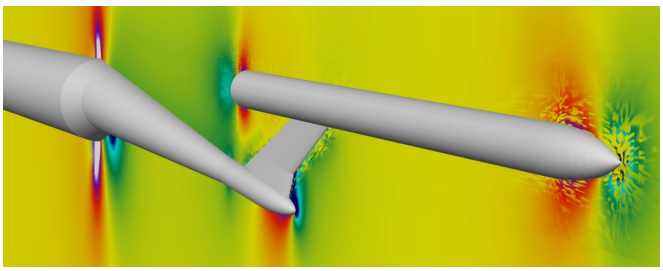

Figure 10: Euler Chimera computation of the sting calibration body mounted on Z-sting and blade at Mach 0.85 and AoA 0º: Mach number in the plane of symmetry

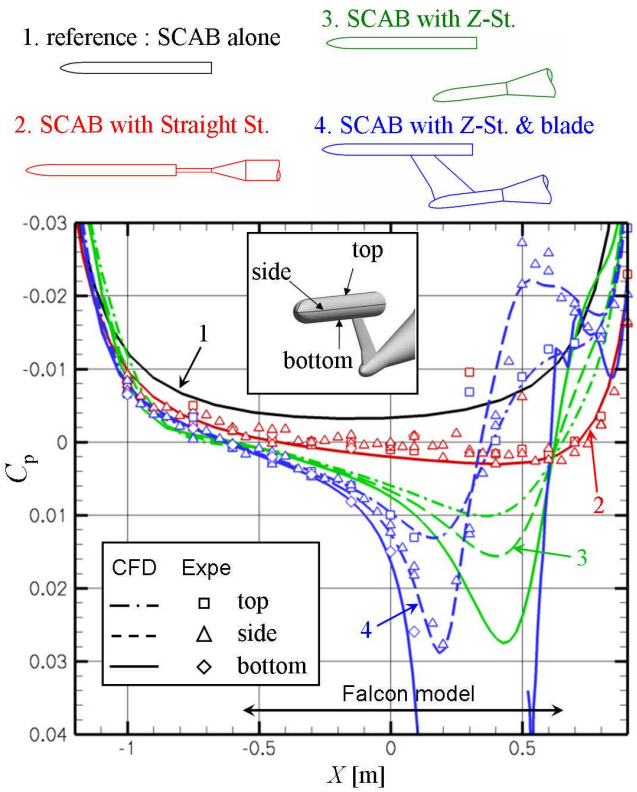

Figure 11: Pressure distribution on the calibration body for various sting supports (see on top) at $M_\infty = 0.85$ and $\alpha_\infty = 0º$, computed by Euler CFD (lines) and measured (symbols)

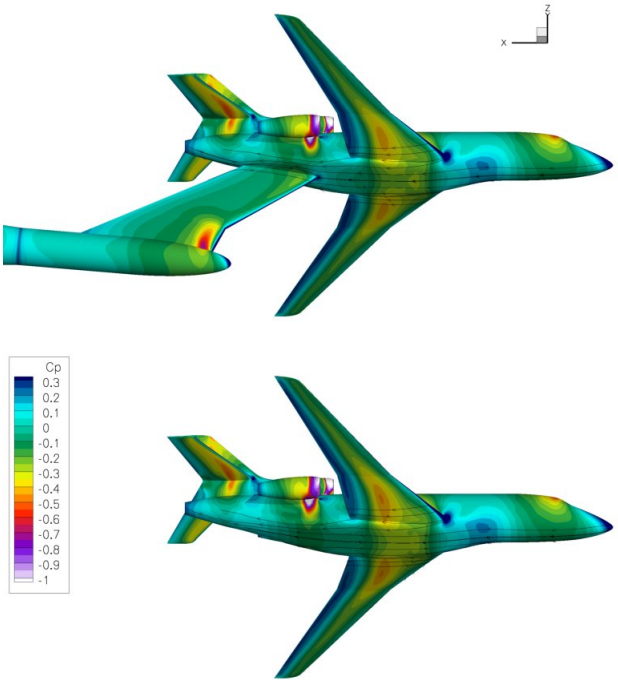

Figure 12: Pressure distribution and friction lines under the Falcon model with (top) and without (bottom) Z-sting support

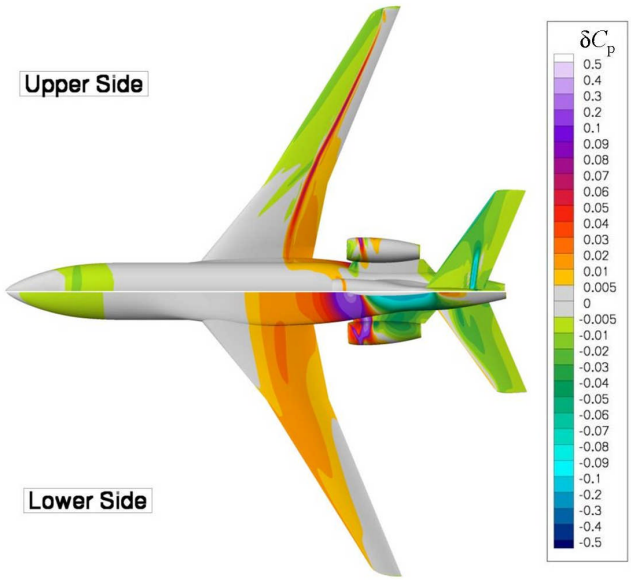

Figure 13: Sting effect on pressure distribution on the Falcon model

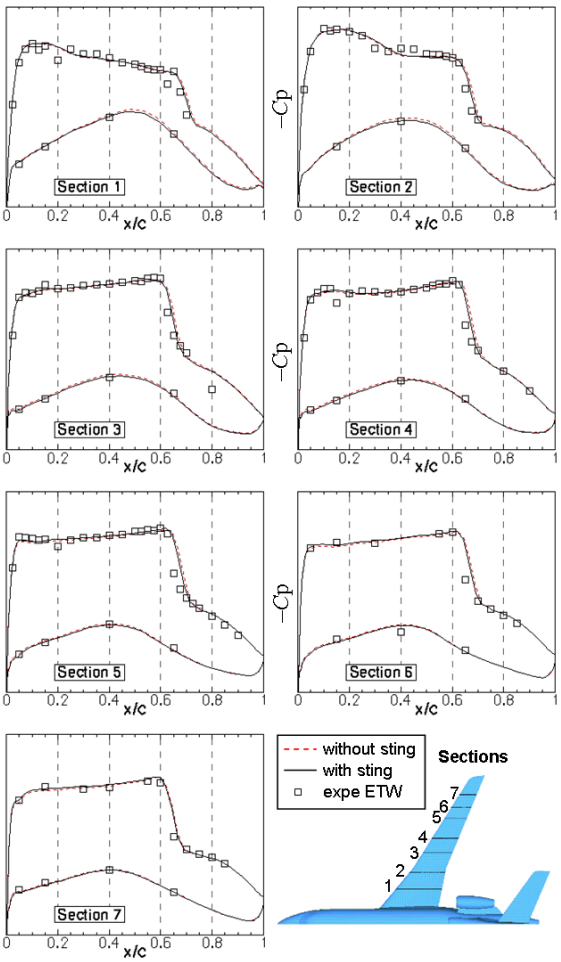

Figure 14: Wing pressure distribution on the Falcon model

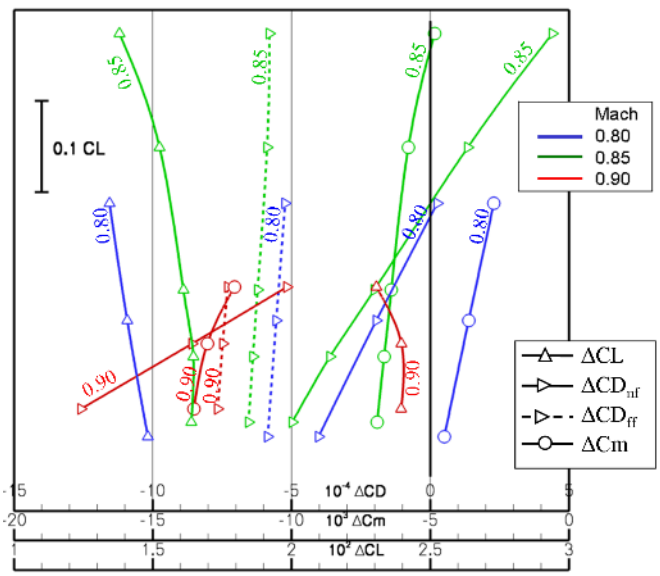

Figure 15: Sting effect on force coefficients